



OPEN

Ultrafast propagation of β -amyloid fibrils in oligomeric cloud

SUBJECT AREAS:
BIOCHEMICAL ASSAYS
PROTEIN AGGREGATIONHirotugu Ogi¹, Masahiko Fukukshima¹, Hiroki Hamada¹, Kentaro Noi¹, Masahiko Hirao¹, Hisashi Yagi^{2*} & Yuji Goto²Received
11 July 2014Accepted
22 October 2014Published
7 November 2014Correspondence and
requests for materials
should be addressed to
H.O. (ogi@me.es.
osaka-u.ac.jp)* Current address:
Center for Research on
Green Sustainable
Chemistry, Tottori
University, 4-101
Koyama-cho minami,
Tottori, Tottori 680-
8550, Japan.¹Graduate School of Engineering Science, Osaka University, Toyonaka, Osaka 560-8531, Japan, ²Institute for Protein Research, Osaka University, Yamadaoka 3-2, Suita, Osaka 565-0871, Japan.

Interaction between monomer peptides and seeds is essential for clarifying the fibrillation mechanism of amyloid β ($A\beta$) peptides. We monitored the deposition reaction of $A\beta_{1-40}$ peptides on immobilized seeds grown from $A\beta_{1-42}$, which caused formation of oligomers in the early stage. The deposition reaction and fibrillation procedure were monitored throughout by novel total-internal-reflection-fluorescence microscopy with a quartz-crystal microbalance (TIRFM-QCM) system. This system allows simultaneous evaluation of the amount of deposited peptides on the surface seeds by QCM and fibril nucleation and elongation by TIRFM. Most fibrils reached other nuclei, forming the fibril network across the nucleus hubs in a short time. We found a fibril-elongation rate two-orders-of-magnitude higher in an oligomeric cloud than reported values, indicating ultrafast transition of oligomers into fibrils.

Aggregation phenomenon of $A\beta$ peptides is highly associated with pathogenesis of Alzheimer's disease (AD)^{1,2}. There are two major $A\beta$ peptides, known as $A\beta_{1-40}$ and $A\beta_{1-42}$, and their aggregation pathways have been studied intensively. They experience several intermediates, including small oligomers, micelles, and protofibrils, to form well-oriented fibrils composed of β -sheet structures³⁻⁶. Most previous studies focused on their nucleation and aggregation behaviors in bulk solutions, where interactions among the intermediates dominate the aggregation reaction. However, recent studies have shown a series of evidence that deposition of the $A\beta$ peptides on immobilized seeds in membranes leads to forming of neurotoxic structures⁷⁻⁹. For example, Yanagisawa *et al.*¹⁰ observed $A\beta$ peptides attached to monosialoganglioside GM1 in AD brains, which could act as immobilized $A\beta$ seeds for triggering acceleration of deposition of $A\beta$ peptides¹¹⁻¹³. Thus, a methodology for monitoring the deposition reaction of $A\beta$ monomers on seeds immobilized on the surface is the key for understanding the substantive pathogenic mechanism of AD. (The role of the membranes is not only the creation of the seeds, but also the formation of toxic fibrils, whose structures are different from those in solution¹¹.) Several methods were proposed for this purpose, including quartz-crystal microbalance (QCM) biosensors¹⁴, surface-plasmon-resonance biosensors¹⁵, and dual-polarization interferometry¹⁶. However, these methods cannot monitor the fibrillation process visually and force us to make ambiguous hypotheses for the aggregation mechanism from the macroscopic indirect observations. Also, they monitor the deposition behaviors for only a short time because of instrument restriction^{14,17} and fail to detect an important event after a long lag time, which is a representative thermodynamic aspect of aggregation reactions of amyloidosis peptides¹⁸⁻²⁰. Direct observations of fibril elongation were performed by total-internal-reflection-fluorescence microscopy (TIRFM)²¹⁻²⁴ and atomic-force microscopy (AFM)²⁵⁻³⁰. Although these methods allow real-time monitoring of fibril growth, they fail to perform through-monitoring including nucleation after a long lag time and elongation of fibrils because of their limited measurement times with stagnant solutions. The through-monitoring including nucleation and growth of fibrils is essential for studying structural transformation from the intermediates into protofibrils.

Therefore, simultaneous measurement of the quantitative amount of deposited peptides and real-time imaging of local structural change would be a breakthrough for understanding the essence of evolution of the peptides on the surface. In this study, we develop a novel TIRFM-QCM system, which allows the real-time monitoring of fibrillation visually with TIRFM and the amount of deposited peptides on seeds with a wireless-electrodeless QCM. We recently established wireless-electrodeless QCM biosensors for achieving ultrahigh-sensitive detection of specific proteins and studied interactions among proteins³¹. It has been unrealistic to integrate a label-free biosensor into TIRFM because usual biosensor chips possess metallic coatings for protein immobilization, through which the TIRF observation becomes difficult. On the other hand, our wireless-electrodeless QCM



causes no difficulty in this issue because of perfect transparency of naked quartz. Proteins adsorb on naked quartz surface with high affinity³². Thus, TIRFM-QCM is the only method that combines TIRFM and a label-free biosensor.

Previously, the deposition reactions of $A\beta$ peptides on their various seeds, including heterogenous seeds, were studied systematically with a wireless-electrodeless QCM biosensor, revealing that $A\beta_{1-40}$ peptides accumulate on $A\beta_{1-42}$ seeds grown at a low pH to form oligomeric structures with a high deposition rate³³. We focus principally on this binding system because it can be an important model for AD³³. A steady flow of $A\beta_{1-40}$ -peptide solution was made to cause the deposition reaction on the sensor surface, on which the ultrafast fibrillation event was observed in real time through the thioflavin T (ThT) fluorescence assay as well as the QCM mass measurement.

Here, we show that deposition of $A\beta_{1-40}$ peptides on the $A\beta_{1-42}$ seeds produces a significant oligomeric cloud on the surface in the early stage, where few fibrils appear, and after deceleration of the peptide-deposition reaction, fibrils grow from newly created nuclei, elongate up to $\sim 4 \mu\text{m}$, and reach other nuclei to achieve the fibril network across the nucleus hubs. This fibril-network formation immediately propagates over the entire region, and it is completed in a short time. The single-fibril elongation rate was larger than reported values by a factor exceeding 100. Such an ultrafast fibril growth indicates a transition of oligomers into fibrils.

Results

TIRFM-QCM system. Developing the TIRFM-QCM system depended crucially on the transmissive quartz-crystal sensor chip as shown in Supplementary Fig. 1a. A $28.5\text{-}\mu\text{m}$ -thick naked AT-cut quartz plate with $1.7 \times 2.5 \text{ mm}^2$ area was set on a cover glass, which took up a part of the bottom wall of the flow channel. A pair of line antennas was located above the flow channel, which generated and detected the pure-shear vibrations of the quartz resonator contactlessly by the electromagnetic waves. The TIRF observation was performed from the bottom through the cover glass using the ThT fluorescence characteristic for β -sheet structures (Methods). The flow rate was $200 \mu\text{l}/\text{min}$ (the flow velocity above the quartz was about $1 \text{ mm}/\text{s}$). The measured resonance spectrum was good even during solution flow (Supplementary Fig. 1b). We performed the TIRFM-QCM experiments at room temperature.

Accumulation behavior of $A\beta_{1-40}$ peptides on immobilized $A\beta_{1-42}$ seeds. In this paper, we use the term *seeds* for aggregates, which are initially immobilized on the quartz sensor chip, and the term *nuclei* for origins of $A\beta_{1-40}$ fibrils, which are generated during the deposition reaction in the oligomeric cloud. Seeds and nuclei are both ThT positive.

$A\beta_{1-42}$ seeds grown at pH 4.6 were immobilized on the quartz surface, and the $A\beta_{1-40}$ peptide solution (10 or $30 \mu\text{M}$, pH 7.4) was flowed. (As described above, this deposition system promotes formation of oligomers.) The solution was circulated for a long-time measurement, but we observed no fibrils and large aggregates in the flowing solution by atomic-force microscopy (AFM) and TIRFM after the measurements. The ThT-fluorescence level of the flowing solution remained unchanged from the baseline even after 10 h, indicating that $A\beta_{1-40}$ peptides in the flowing solution do not show the cross- β -sheet characteristic of amyloid fibrils. (Because ThT is insensitive to non-cross- β oligomers, the ThT-negative solution does not mean a monomeric peptide solution: The flowing solution could involve ThT-negative small oligomers, although we could not find them with our AFM method.)

Figure 1a shows time courses of the amount of deposited $A\beta_{1-40}$ peptides on the quartz surface obtained from the QCM measurement. The frequency responses were unstable compared with a typical QCM measurement for an antigen-antibody interaction because

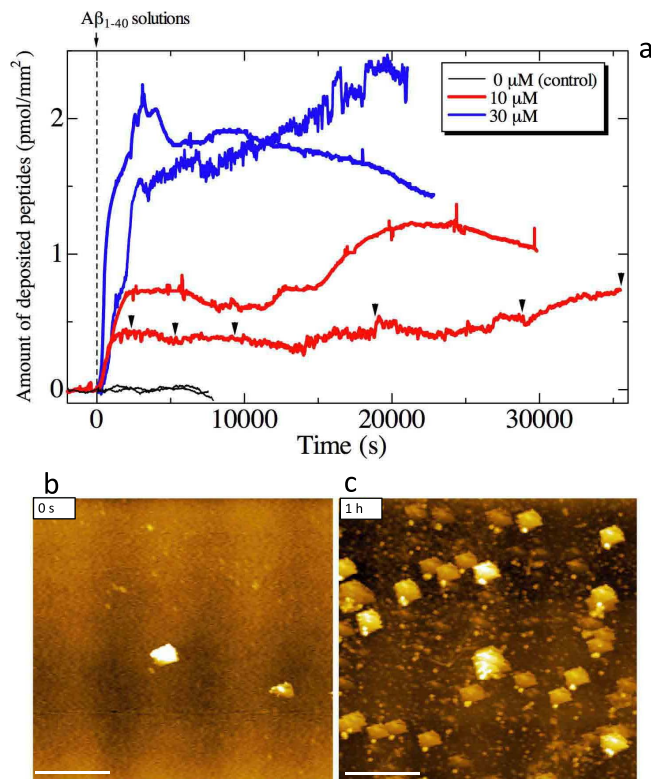


Figure 1 | Monitoring deposition reactions. (a) The resonance frequency ($\sim 58 \text{ MHz}$) of the quartz resonator was monitored during the deposition reaction of $A\beta_{1-40}$ peptides, which yielded the amount of accumulated peptides on the surface. The peptides quickly accumulate on the surface-immobilized $A\beta_{1-42}$ seeds just after the reaction. Two independent measurements are shown for each peptide concentration. Black inverted triangles indicate the time at which the TIRFM images are shown in Fig. 2a–2g. (b) An AFM image on the quartz surface before the deposition reaction, and (c) that after 1 h for a $10\text{-}\mu\text{M}$ - $A\beta_{1-40}$ solution-flow measurement. The scale bars indicate $2 \mu\text{m}$.

of the ongoing TIRF observation. However, these results clearly demonstrate that the $A\beta_{1-40}$ peptides are markedly deposited on the surface-immobilized $A\beta_{1-42}$ seeds within $\sim 1 \text{ h}$ and then the deposition reaction slows. (Degradation of the deposition rate was also observed in the previous study³³, which may be attributed to temporarily occupied active sites on the seeds by the accumulated peptides.) The higher the peptide concentration, the larger the amount of deposition. We studied the quartz surface by AFM and found that the surface roughness before the solution flow (Fig. 1b) ($< \sim 0.5 \text{ nm}$) increased considerably ($> \sim 1.5 \text{ nm}$) after 1 h from the solution arrival, where many particles were observed with few fibrils (Fig. 1c).

Nucleation and fibril-network formation. Figures 2a–2g show changes in the TIRFM image as the deposition reaction proceeds; they correspond to the solution-flow measurement with $10 \mu\text{M}$ indicated by black inverted triangles in Fig. 1a. Importantly, few fibrils were observed until $\sim 5000 \text{ s}$ (Fig. 2a–2c), despite significant progress in the deposition reaction during this period, which is confirmed by the QCM response. (The small ThT-positive particles in Fig. 2a represent the $A\beta_{1-42}$ seeds and they remain throughout the measurements.) This indicates that the deposited peptides do not metamorphose into the cross- β sheet structures but cause oligomeric aggregates, although ThT is insensitive to non-cross- β structures and it fails to identify the oligomer structure. Oligomeric structures were principally observed by the AFM after 1 h (Fig. 1c). After a long stable period, nuclei of $A\beta_{1-40}$

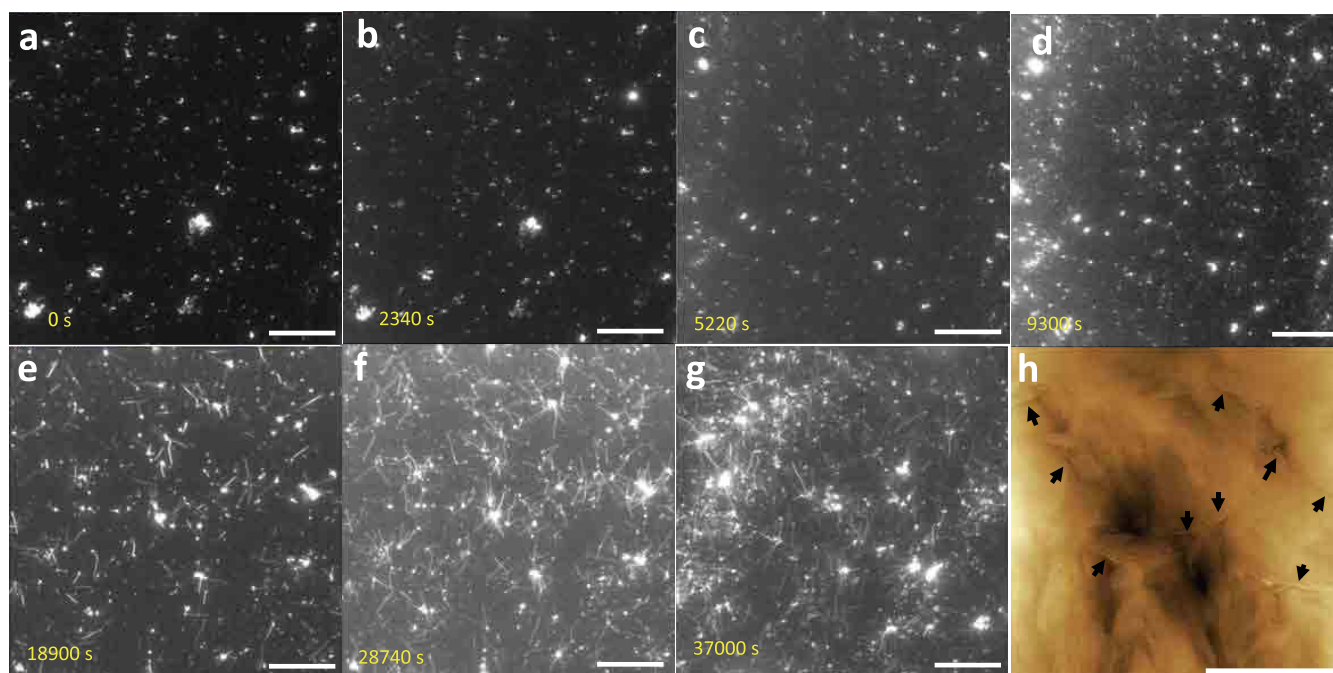


Figure 2 | Time course of fibrillation on surface. (a–g) TIRFM images at several stages of the 10- μM - $A\beta_{1-40}$ solution-flow measurement indicated by black inverted triangles in Fig. 1a. No fibrillation occurs until ~ 5000 s despite significant progress of peptide deposition. Dense fibril networks are, however, quickly formed in the later stage. The scale bars indicate 10 μm . (h) An AFM image on the quartz surface after the deposition measurement, showing fibrils embedded in the oligomeric clouds indicated by black arrows. The scale bar indicates 1 μm .

were created and a small number of fibrils were observed (Fig. 2d), and then, intensive fibril origination and elongation from nuclei occurred (Fig. 2e–2g and Supplementary Movie 1). We digitally evaluated the evolution of the amount of surface fibrils observed by the TIRFM (Supplementary Fig. 2a and 2b), which dramatically rose in this later stage (Supplementary Fig. 2c); this corresponds to the well-known phenomenon of fibrillation after a long lag time³⁴. Figure 2h shows an AFM image on the quartz chip after the deposition-reaction measurement (at ~ 40000 s), indicating fibril growth inside the oligomeric cloud.

Formation of fibril network. As shown in the Supplementary Movies, fibrils originate at nuclei. They elongate step-wisely as reported previously^{21,22,28,29}. However, their growth rates under these conditions of continual $A\beta_{1-40}$ flow over immobilized $A\beta_{1-42}$ seeds are dramatically larger than previous reports (Table 1). Figure 3 shows snapshots of the TIRFM images at later stages, displaying ultrafast fibril-growth behavior. As shown in Fig. 3a and Supplementary Movie 2, some fibrils elongated with significantly large growth rates ($> \sim 10$ $\mu\text{m}/\text{s}$). The largest growth rate among previous studies was ~ 0.1 $\mu\text{m}/\text{s}$, which was determined by AFM²⁸. Figure 4 shows histograms for fibril length and fibril-growth rate. Fibrils are not observed to be larger than ~ 10 μm (Fig. 4a), as the fibril length is limited to the average distance between nuclei, because fibrils originated from nucleus eventually terminate at other nucleus in the dense fiber network of the sample. The average growth rate was 4 $\mu\text{m}/\text{s}$, and the maximum rate exceeds 10 $\mu\text{m}/\text{s}$ (Fig. 4b), being larger than previous reports by factors exceeding 100.

For comparison, we made similar measurements using $A\beta_{1-40}$ seeds immobilized on the surface instead of $A\beta_{1-42}$ seeds. In this case, however, we did not observe an ultrafast fibril elongation; the fibrils appeared and grew just after the solution flow as shown in Supplementary Fig. 2c and Supplementary Fig. 4. Therefore, ultrafast elongation will be only observed inside the oligomer cloud.

Also a striking observation is that many fibrils originated from nuclei eventually come at other nuclei as shown in Fig. 3b–3d and

Supplementary Movies 3–5. This nucleus-bridging phenomenon propagates and the fibril network on nucleus hubs is formed in a short time (Supplementary Fig. 3). The fibrils appeared from nuclei, not from the initially immobilized seeds in the case of the deposition reaction on the $A\beta_{1-42}$ seeds. Supplementary Movie 6 shows the nucleation phenomenon during the solution flow in real time, where small particles appear, indicating nuclei. On the other hand, fibrils principally elongated from the surface-immobilized seeds for the heterogeneous deposition reaction on the $A\beta_{1-40}$ seeds (Supplementary Figure 4).

Furthermore, we studied the effect of the solution flow on the elongation rate. In the case of the same $A\beta_{1-40}$ concentration (10 μM) and the same pH (7.4) on the $A\beta_{1-42}$ seeds, we failed to observe any noticeable fibrillation even over 10 h without solution flow. Then, we searched for experimental conditions for the real-time fibril-growth observation in a non-flow environment. The condition we found was a higher peptide concentration (40 μM) at lower pH (pH 2.4) on $A\beta_{1-40}$ seeds grown at pH 2.4. In this case, the fibril elongation rate was very low (~ 4 nm/s) as shown in Supplementary Figure 5 and Supplementary Movie 7, being comparable with previous studies. Note that all previous studies for the direct monitoring of fibril elongation were performed in stagnant solutions without flow. Thus, these experiments support the importance of the $A\beta_{1-40}$ oligomer layer formed in the solution flow.

Discussion

Remarkable observations are (i) ultrafast fibril elongation, (ii) step-wise and limited growth, and (iii) bridging fibril between nuclei. To explain these, we propose a model based on the conformational conversion of oligomer into oriented β -sheet structure for fibril growth (Fig. 5).

The QCM measurement clearly indicates the deposition of the peptides in the early stage, and the TIRFM measurement shows that this deposited layer is negative to ThT, which we call the oligomer cloud. The oligomer cloud will involve both nonspecifically adsorbed $A\beta_{1-40}$ peptides on the quartz surface and those specifically accumu-



Table 1 | Fibril elongation rates

	method	rate (nm/s)	protein
present	TIRFM-QCM	$<\sim 10000$	$A\beta_{1-40}$
Kellermayer <i>et al.</i> ²⁸	AFM	$<\sim 100$	$A\beta_{25-35}$
Milhiet <i>et al.</i> ²⁹	AFM	~ 60	lithostathine
Ferkinghoff-Borg <i>et al.</i> ²³	TIRFM	$<\sim 20$	glucagon
Ban <i>et al.</i> ²¹	TIRFM	$<\sim 8$	$A\beta_{1-40}$
Qiang <i>et al.</i> ³⁰	AFM	$<\sim 1.8$	$A\beta_{1-40}$
Sharadrao <i>et al.</i> ²⁴	TIRFM	$<\sim 0.65$	amylin
Goldsbury <i>et al.</i> ²⁷	AFM	~ 0.3	$A\beta_{1-40}$
Green <i>et al.</i> ²⁶	AFM	~ 0.02	human amylin
Pinotsi <i>et al.</i> ³⁵	super-resolution microscopy	$<\sim 0.01$	α -synuclein

lated on the $A\beta_{1-42}$ seeds. However, the latter should be important for the ultrafast fibril elongation phenomenon, because in the case of the deposition reaction on the $A\beta_{1-40}$ seeds, fibril growth from the seeds was observed at an early stage as displayed in Supplementary Figures 2c and 4, and we failed to observe ultrafast elongation. It has been indicated that an $A\beta$ fibril grown from a seed inherits its molecular structure from that of the seed³⁶, and this may explain the formation of the oligomer cloud at the beginning of the deposition reaction: The $A\beta_{1-42}$ seeds show similar templates to those of

$A\beta_{1-40}$ fibrils and capture the $A\beta_{1-40}$ peptides efficiently. However, because of the different templates, the deposited $A\beta_{1-40}$ peptides form not specific ordered structures but disordered aggregates (Fig. 5b), taking a long time for nucleation and fibrillation. After the lag time, the nuclei are generated, being associated with interactions between oligomers and flowing peptides, from such regions that are close to β -sheet structures; because the oligomeric cloud consists of various structures, some regions exhibit similar structures to β -sheet structures. Origin of the nucleus will constrain the

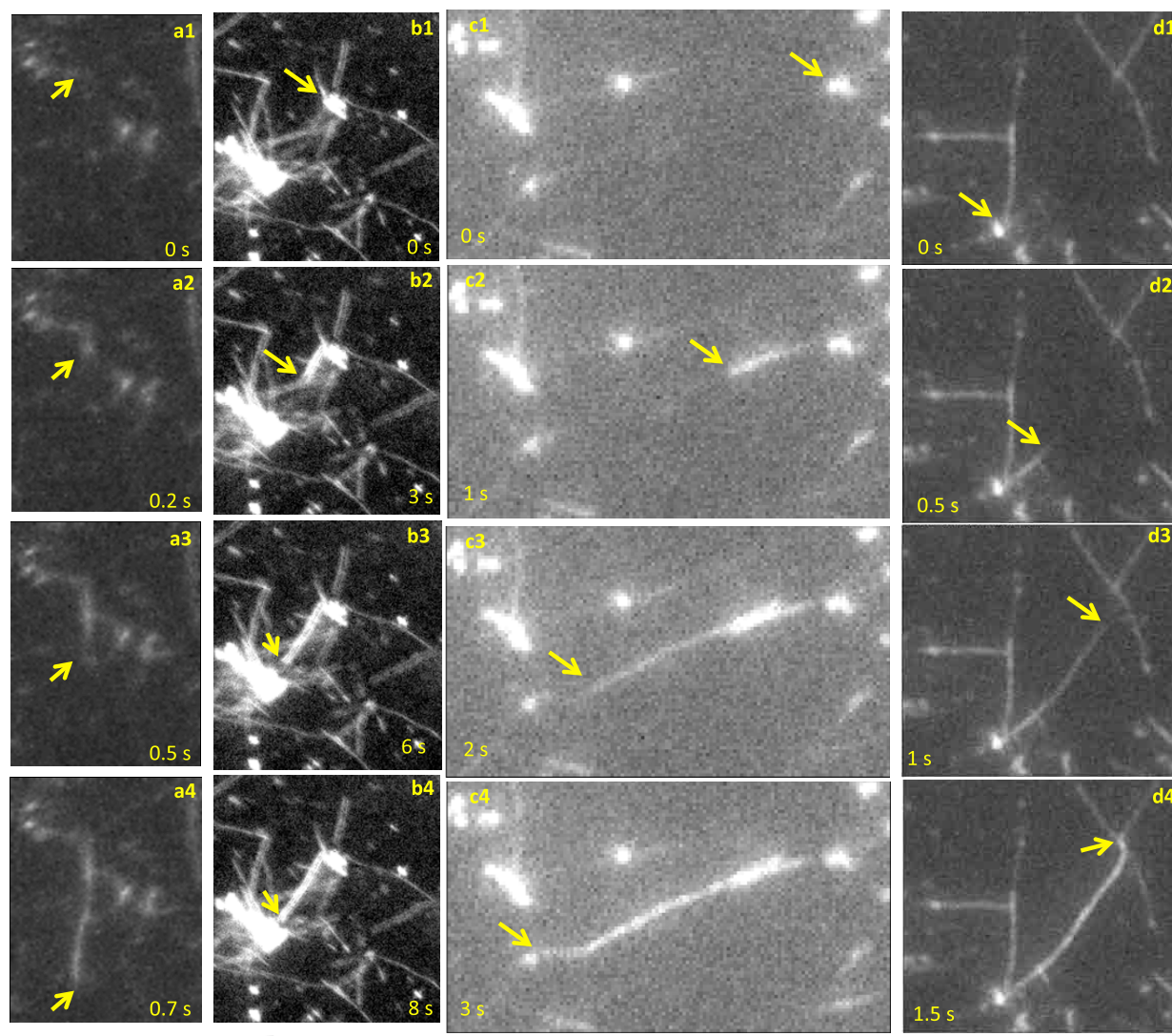


Figure 3 | Snapshots of fibril growth behaviors. (a) ultrafast fibril elongation, and (b–d) fibril origination from nuclei and their attachment to the neighbor nuclei in the flow measurement of $10\ \mu\text{M}$ $A\beta_{1-40}$ on the $A\beta_{1-42}$ seeds. The scale bars indicate $5\ \mu\text{m}$.

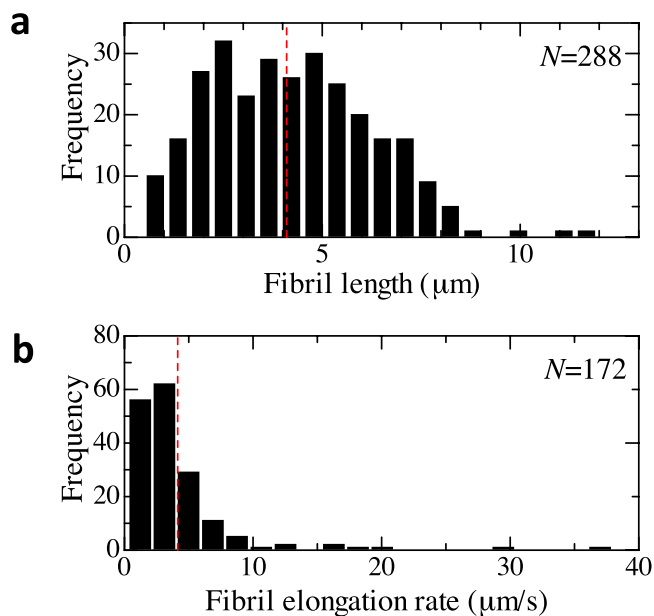


Figure 4 | Histograms for fibril length and growth rate. (a) and (b) show histograms of fibril length and fibril elongation rate in the solution-flow measurement ($10 \mu\text{M } A\beta_{1-40}$), respectively. The fibril length was measured by the segmented-line mode of the image J. The growth rate was evaluated for fibrils, which originated from and reached nuclei, by dividing the fibril length by the time needed to reach the other nucleus.

surrounding oligomers to prepare for transformation into fibrils, and the oligomers near the nucleus will be distorted for the conversion into β -sheet structures (Fig. 5c). Triggered by the nucleation, the fibril immediately grows, being accompanied by the conversion of oligomers, and it comes at another nucleus because of the close structures to fibrils around it. The fibril length is thus limited to be the average distance between nuclei.

The conversion of oligomer into fibril has been often pointed out³⁷, and it has been suggested that amyloid fibrils grow efficiently through the conversion of oligomers at the fibril ends³⁸. Therefore, it is convincing that fibrils grow in the oligomeric cloud in connection with the conformational conversion, because this makes the extraordinarily fast elongation possible. It will be difficult to achieve such a

high elongation rate with diffusion-controlled fibril elongation mechanism, which requires longer time for peptides to cause diffusion to the fibril ends and then to interact and attach there. Actually, the elongation rate was significantly smaller ($< \sim 0.01 \mu\text{m/s}$) in previous studies^{21,27} even for the same peptide as the present study, indicating that the diffusion-controlled-elongation mechanism was dominant in those studies because of absence of surrounding oligomers. We attribute the stepwise elongation to stepwise conversion behavior; when the fibril reaches highly misoriented oligomer structure, its growth will stop until the conversion there completes.

Another possible mechanism is precipitation from supersaturation, which is a recently proposed concept for explaining fibrillation behavior, being analogous to crystallization¹⁸. If the oligomeric cloud could trap $A\beta_{1-40}$ monomers like as a cage and produce supersaturation regions locally, an ultrafast fibril elongation will occur based on the precipitation phenomenon from supersaturation. At this moment, however, there is no direct experimental data supporting this mechanism, and it remains hypothesis.

We showed that the fibril elongation rate evaluated here was much larger than that reported. This value could be even larger, because we evaluated it using the ThT fluorescence assay: A longer time is required for ThT molecules to recognize newly created fibrils via diffusion and attach to them. In other words, the observed rate of fibril growth was rate-limited by ThT fluorescence assay. Many fibrils were first recognized as dark lines and then they are brightly illuminated as shown in Supplementary Fig. 6. This phenomenon indicates that ThT molecules in the flowing solution move to newly created cross- β strands and cause their conformation change for fluorescence. The time needed to recognize fibrils, move to them, and ThT conformation change for fluorescence is the minimum time for sensing in this study.

Methods

Development of TIRFM-QCM. Supplementary Fig. 1a shows a cross-section of the TIRFM-QCM. Two line antennas with 1-mm diameters were set in parallel above the AT-cut quartz plate. Tone bursts with $\sim 1000 \text{ V}$ amplitude and $5 \mu\text{s}$ duration were applied to the generation antenna, which launched the electromagnetic wave towards the quartz to cause pure-shear vibration via the converse piezoelectric effect. Even after the excitation, the vibration of the quartz continued, generating another electromagnetic wave via the piezoelectric effect, which was detected by the receiving line antenna, and the received signal was fed to a superheterodyne spectrometer (RITEC, RAM-10000). By sweeping the frequency of the tone bursts and getting the amplitude of the detected signal, the resonance spectrum as shown in the

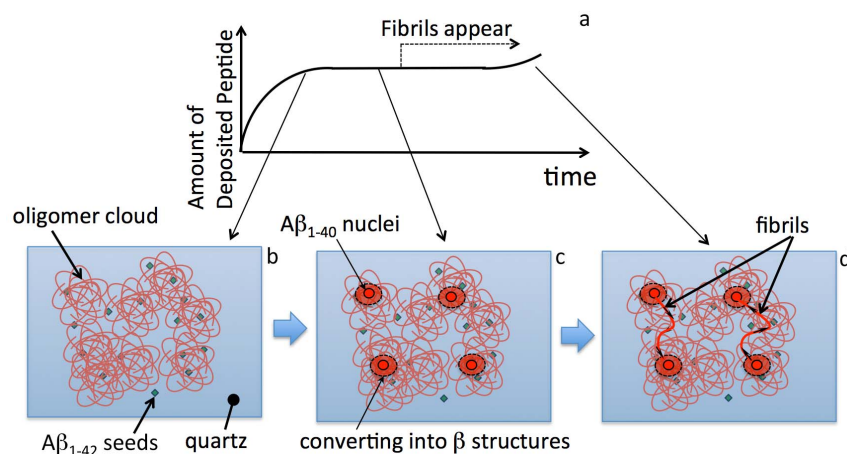


Figure 5 | The oligomer-conversion-assisted ultrafast-fibril elongation model. (a) Schematic of time course of amount of deposited peptides on surface. (b) The $A\beta_{1-40}$ peptides are adsorbed at surface-immobilized $A\beta_{1-42}$ seeds, forming the oligomeric cloud. (c) Nuclei are generated in oligomer cloud after a long lag time. Structures of oligomers near the nuclei are affected so as to cause β -sheet structure. (d) Fibrils quickly grow from the nuclei, causing conformational conversion of oligomers into fibrils. They are guided to come at the other nuclei, where oligomer structures are ready to convert into fibrils because of strain field caused by the nuclei.



Supplementary Fig. 1b was obtained. Because the magnitude of the detected vibrational signal depends on the in-plane direction of the exciting electric field to the crystallographic axis of quartz, the in-plane angle of the quartz chip was adjusted to obtain the maximum peak amplitude. Once the resonance spectrum was obtained, the change in the resonance frequency was monitored through the change in the phase at fixed peak frequency³⁹. Thus, noncontacting measurement of the electrodeless quartz resonator was performed. Solution flow was made by a pump unit (Shimadzu, LC-20AD) with degasifier (Shimadzu, DGU-20A3) and diversion valve (Shimadzu, FCV-13AC).

The TIRF system was developed principally using optics by Nikon (ECLIPSE Ti). The light source was a mercury lamp (KEYENCE, VB-L10), and a single-band color-filter set was used (Semrock, CFP-2432C-NTE) for making a pumping light of 438 ± 12 nm for exciting ThT molecules in the evanescent field on the quartz surface through a $\times 60$ objective lens and for detecting 483 ± 16 nm fluorescence light by a vacuum-cooled CMOS camera (Andor, Neo sCMOS, DC-152Q-C00-FI) at the cooling of -30°C . The minimum frame rate was 0.1 s.

Analysis of QCM data. The amount of deposited peptides in a unit area on the quartz chip, σ , in Fig. 1 was calculated from the fractional change in the resonance frequency $\Delta f/f$ of the quartz using the Sauerbrey equation⁴⁰.

$$\sigma = -\frac{\Delta f}{f} \frac{d_q \rho_q}{M_w} \quad (1)$$

Here d_q and ρ_q are thickness and mass density of the quartz resonator, respectively, and M_w denotes the molecular mass.

ThT fluorescence assay. ThT is essentially non-fluorescent in solution and becomes fluorescent only when it attaches to the cross- β sheet conformation of amyloid fibrils. ThT fluorescence assay has been extensively used for evaluating protofibrils and their extension. We measured the ThT level of the seed solution and the flowing solution as follows. A stock solution for ThT assay was prepared by dissolving ThT (Wako, 202-01002) in a glycine/sodium-hydroxide buffer solution (pH 8.5) with a final concentration of 5 μM . A 100 μl sample solution was mixed with 1 ml of the stock solution, and the mixture solution was poured into a quartz-glass cell for the fluorospectrophotometer (JASCO, FP-6200). The ThT fluorescence level was measured as the fluorescence at 490 nm with the excitation at 450 nm.

Preparation of $A\beta_{1-42}$ seeds. The lyophilized $A\beta_{1-42}$ peptides (Peptide Institute, 4349-v) were dissolved in dimethyl sulfoxide (DMSO) (Wako, 049-07213) and diluted to a concentration of 50 μM by an acetate buffer solution (ABS) with 0.1 M NaCl and pH 4.6 (Fluka, 31048-1L). (DMSO:ABS = 1 : 4). This solution was stirred at 1200 rpm for 18 h to make seeds. (At this stage, the ThT level was 100–150, much higher than the baseline value about 5). This seed solution was then sonicated for 1 min with a 200-kHz high-power ultrasonic generator (KAIJO, 4021). A ThT solution (100- μM ThT in glycine/sodium-hydroxide buffer solution) was added to the seed solution to obtain the final seed solution containing 10- μM $A\beta_{1-42}$ and 80 μM ThT.

The AT-cut quartz plate was immersed in a piranha solution (98% H_2SO_4 :33% $\text{H}_2\text{O}_2 = 4 : 1$) for 30 min and rinsed with ultrapure water. Then, it was set in the flow channel and the seed solution was injected. After incubation for 3 h at 4°C , the flow cell was set on the TIRF stage (Supplementary Fig. 1a). As shown in Figs. 1b and 2a, ThT-positive seed particles ($< \sim 1$ μm) were immobilized on the quartz surface. No obvious fibrils were observed with AFM and TIRFM for the immobilized seeds; they are granular aggregates with the cross- β -sheet structures, but not composed of well-oriented fibrils.

Flow measurement. The solution for flow containing $A\beta_{1-40}$ peptides was prepared by dissolving the lyophilized $A\beta_{1-40}$ peptides (Peptide Institute, 4307-v) in DMSO and diluting it with ultrapure water (DMSO:ultrapure water = 1 : 19). The ThT solution was then added to obtain the solution for flow containing 10 or 30 μM $A\beta_{1-40}$ and 60 μM ThT. The buffer solution (without $A\beta_{1-40}$ peptides) was first flowed for obtaining the stable baseline of the resonance frequency less than 1 ppm (typically for 1 h), and then the peptide solution was flowed to the sensor cell and circulated for long-time measurement. Because the solution contains 5% DMSO, we expect that the $A\beta_{1-40}$ peptides are isolated (monomers), although we do not confirm this.

Non-flow measurement. The lyophilized $A\beta_{1-40}$ peptides (Peptide Institute, 4307-v) were dissolved in DMSO and diluted to achieve a final concentration of 50 μM by a glycine-HCl buffer (GHB) with 0.1-M NaCl and pH 2.4 (Wako, 077-04711) (DMSO:GHB = 1 : 4). This solution was stirred at 1200 rpm for 3 h to make the seeds. At this stage, the ThT level was about 100. The ThT solution was added to the seed solution to obtain the final seed solution containing 40 μM $A\beta_{1-40}$ and 80 μM ThT.

The quartz plate was immersed in the piranha solution for 10 min and rinsed with ultrapure water. A drop of the seed solution was put on the quartz surface and incubated for 3 h. The solution was removed by a Kimwipe paper and the surface was rinsed with ultrapure water. The quartz plate was then set in the sensor cell.

The peptide solution of $A\beta_{1-40}$ was prepared by dissolving the lyophilized $A\beta_{1-40}$ peptides in DMSO and diluting it with GHB and the ThT solution to obtain final

concentrations of 40 μM $A\beta_{1-40}$ and 20 μM ThT. This solution was injected into the sensor cell and the QCM and TIRF measurements were performed without making flow.

Analysis of TIRFM images. Using Image J ver 1.46r (produced by National Institute of Health, USA), we evaluated the average fibril length per unit area in the TIRFM images. Obtained images were converted to 8-bit images and binarized by setting thresholds (Supplementary Figs. 2a and 2b), where the upper thresholds were set so as to remove large aggregates, which existed from the start. In the particle counting procedure, we removed particles, whose area is smaller than 100 nm^2 for focusing newly created fibrils. The fibril occupation area was then computed.

AFM measurement. AFM observation was performed on the quartz surface before and after the measurements. The tapping-mode measurement was used with a silicon cantilever (stiffness of 40 N/m) with the resonance frequency near 300 kHz. The scan frequency was 0.5 Hz. The instrument was produced by Shimadzu Co. Ltd. (SPM A9600).

- Lambert, M. P. *et al.* Diffusible, nonfibrillar ligands derived from $A\beta_{1-42}$ are potent central nervous system neurotoxins. *Proc. Natl. Acad. Sci. USA* **95**, 6448–6453 (2003).
- Bucciantini, M. *et al.* Inherent toxicity of aggregates implies a common mechanism for protein misfolding diseases. *Nature* **416**, 507511 (2002).
- Bernstein, S. L. *et al.* Amyloid- β protein oligomerization and the importance of tetramers and dodecamers in the aetiology of Alzheimer's disease. *Nat. Chem.* **1**, 326–331 (2009).
- Lee, J., Culyba, E. K., Powers, E. T. & Kelly, J. W. Amyloid- β forms fibrils by nucleated conformational conversion of oligomers. *Nat. Chem. Biol.* **7**, 602–609 (2011).
- Krishnan, R. *et al.* Conserved features of intermediates in amyloid assembly determine their benign or toxic states. *Proc. Natl. Acad. Sci. USA* **109**, 11172–11177 (2012).
- Garai, K. & Frieden, C. Quantitative analysis of the time course of $A\beta$ oligomerization and subsequent growth steps using tetramethylrhodamine-labeled $A\beta$. *Proc. Natl. Acad. Sci. USA* **110**, 3321–3326 (2012).
- Kakio, A., Nishimoto, S., Yanagisawa, K., Kozutsumi, Y. & Matsuzaki, K. Interactions of amyloid β -protein with various gangliosides in raft-like membranes: Importance of GM1 ganglioside-bound form as an endogenous seed for Alzheimer amyloid. *Biochemistry* **41**, 7385–7390 (2002).
- Subasinghe, S. *et al.* Cholesterol is necessary both for the toxic effect of $A\beta$ peptides on vascular smooth muscle cells and for $A\beta$ binding to vascular smooth muscle cell membranes. *J. Neurochem.* **84**, 471–479 (2003).
- Yip, C. M., Darabie, A. A. & McLaurin, J. $A\beta_{42}$ -peptide assembly on lipid bilayers. *J. Mol. Biol.* **318**, 97–107 (2002).
- Yanagisawa, K., Odaka, A. & Suzuki, N. GM1 ganglioside-bound amyloid β -protein ($A\beta$): a possible form of preamyloid in Alzheimers disease. *Nat. Med.* **1**, 1062–1066 (1995).
- Matsuzaki, K., Kato, K. & Yanagisawa, K. $A\beta$ polymerization through interaction with membrane gangliosides. *Biochim. Biophys. Acta* **1801**, 868–877 (2010).
- Yanagisawa, K. Pathological significance of ganglioside clusters in Alzheimers disease. *J. Neurochem.* **116**, 806–812 (2011).
- Yanagisawa, K. GM1 ganglioside and the seeding of amyloid in Alzheimer's disease: endogenous seed for Alzheimer amyloid. *Neuroscientist* **11**, 250–260 (2005).
- Sasahara, K., Morigaki, K. & Shinya, K. Effects of membrane interaction and aggregation of amyloid β -peptide on lipid mobility and membrane domain structure. *Phys. Chem. Chem. Phys.* **15**, 8929–8939 (2013).
- Aguiar, M. I. & Small, D. H. Surface plasmon resonance for the analysis of β -amyloid interactions and fibril formation in Alzheimers disease research. *Neurotox. Res.* **7**, 17–27 (2005).
- Zhai, J., Lee, T.-H., Small, D. H. & Aguiar, M. I. Characterization of early stage intermediates in the nucleation phase of $A\beta$ aggregation. *Biochemistry* **51**, 1070–1078 (2012).
- Kawasaki, T., Asaoka, K., Mihara, H. & Okahata, Y. Nonfibrous β -structured aggregation of an $A\beta$ model peptide (Ad-2z) on GM1/DPPC mixed monolayer surfaces. *J. Colloid Int. Sci.* **294**, 295–303 (2006).
- Yoshimura, Y. *et al.* Distinguishing crystal-like amyloid fibrils and glass-like amorphous aggregates from their kinetics of formation. *Proc. Natl. Acad. Sci. USA* **109**, 14446–14451 (2012).
- Yoshimura, Y., So, M., Yagi, H. & Goto, Y. Ultrasonication: An efficient agitation for accelerating the supersaturation-limited amyloid fibrillation of proteins. *Jpn. J. Appl. Phys.* **52**, 07HA01 (2013).
- Uesugi, K. *et al.* Mechanisms of ultrasonically induced fibrillation of amyloid β_{1-40} peptides. *Jpn. J. Appl. Phys.* **52**, 07HE10 (2013).
- Ban, T. *et al.* Direct observation of $A\beta$ amyloid fibril growth and inhibition. *J. Mol. Biol.* **344**, 757–767 (2004).
- Ban, T. *et al.* Stop-and-go kinetics in amyloid fibrillation. *Phys. Rev. E* **82**, 010901(R) (2010).
- Ferkinghoff-Borg, J. *et al.* Real-time and single fibril observation of the formation of amyloid β spherulitic structures. *J. Biol. Chem.* **281**, 33677–33683 (2006).



24. Sharadrao, M. *et al.* Heterogeneous amylin fibril growth mechanisms imaged by total internal reflection fluorescence microscopy. *Biochemistry* **50**, 2808–2819 (2011).
25. Blackley, H. K. L. *et al.* In-situ atomic force microscopy study of β -amyloid fibrillization. *J. Mol. Biol.* **298**, 833–840 (2000).
26. Green, J. D. *et al.* Human amylin oligomer growth and fibril elongation define two distinct phases in amyloid formation. *J. Biol. Chem.* **279**, 2206–12212 (2004).
27. Goldsbury, C. *et al.* Multiple assembly pathways underlie amyloid- β fibril polymorphisms. *J. Mol. Biol.* **352**, 282–298 (2005).
28. Kellermayer, M. Z., Karsai, Á., Benke, M., Soós, K. & Penke, B. Stepwise dynamics of epitaxially growing single amyloid fibrils. *Proc. Natl. Acad. Sci. USA* **105**, 141–144 (2008).
29. Milhiet, P.-E. *et al.* Deciphering the structure, growth and assembly of amyloid-like fibrils using high-speed atomic force microscopy. *PLoS ONE* **5**, e13240 (2010).
30. Qiang, W., Kelley, K. & Tycko, R. Polymorph-specific kinetics and thermodynamics of β -amyloid fibril growth. *J. Am. Chem. Soc.* **135**, 6860–6871 (2013).
31. Ogi, H., Nagai, H., Fukunishi, Y., Hirao, M. & Nishiyama, M. 170-MHz electrodeless quartz crystal microbalance biosensor: Capability and limitation of higher frequency measurement. *Anal. Chem.* **81**, 8068–8073 (2009).
32. Ogi, H., Okamoto, K., Nagai, H., Fukunishi, Y. & Hirao, M. Replacement-free electrodeless quartz crystal microbalance biosensor using nonspecific-adsorption of streptavidin on quartz. *Anal. Chem.* **81**, 4015–4020 (2009).
33. Ogi, H. *et al.* Seed-dependent deposition behavior of A β peptides studied with wireless quartz-crystal-microbalance biosensor. *Anal. Chem.* **83**, 4982–4988 (2011).
34. Huong, V. T. *et al.* Catechol derivatives inhibit the fibril formation of amyloid- β peptides. *J. Biosci. Bioeng.* **109**, 629–634 (2010).
35. Pinotsi, D. *et al.* Direct observation of heterogeneous amyloid fibril growth kinetics via two-color super-resolution microscopy. *Nano Lett.* **14**, 339–345 (2014).
36. Petkova, A. T. *et al.* Self-propagating, molecular-level polymorphism in Alzheimers β -amyloid fibrils. *Science* **307**, 262–265 (2005).
37. Bemporad, F. & Chiti F. Self-propagating, Protein misfolded oligomers: Experimental approaches, mechanism of formation, and structure-toxicity relationships. *Chem. & Biol.* **19**, 315–327 (2012).
38. Serio, T. R. *et al.* Nucleated conformational conversion and the replication of conformational information by a prion determinant. *Science* **289**, 1317–1321 (2000).
39. Ogi, H. *et al.* Concentration dependence of IgG-protein A affinity studied by wireless-electrodeless QCM. *Biosens. Bioelectron.* **22**, 3238–3242 (2007).
40. Sauerbrey, G. Verwendung von Schwingquarzen zur Wägung dünner Schichten und zur Mikrowägung. *Z. Phys.* **155**, 206–222 (1959).

Acknowledgments

This study was supported by the Funding Program for Next Generation World-Leading Researchers (Next Program) by the Cabinet Office, Government of Japan.

Author contributions

H.O. established the TIRFM-QCM, analyzed the data, proposed the fibril elongation model, and wrote the paper. M.F. and H.H. acquired the TIRFM images and frequencies. K.N. and H.Y. assisted in the ThT fluorescence assay. Y.G. proposed the fibril model. M.H. contributed to construction of QCM.

Additional information

Supplementary Information accompanies this paper at <http://www.nature.com/scientificreports>

Competing financial interests: The authors declare no competing financial interests.

How to cite this article: Ogi, H. *et al.* Y. Ultrafast propagation of β -amyloid fibrils in oligomeric cloud. *Sci. Rep.* **4**, 6960; DOI:10.1038/srep06960 (2014).



This work is licensed under a Creative Commons Attribution-NonCommercial-ShareAlike 4.0 International License. The images or other third party material in this article are included in the article's Creative Commons license, unless indicated otherwise in the credit line; if the material is not included under the Creative Commons license, users will need to obtain permission from the license holder in order to reproduce the material. To view a copy of this license, visit <http://creativecommons.org/licenses/by-nc-sa/4.0/>